A Smart Ice Monitoring System for Photovoltaic Applications based on Capacitive Graphene Sensors

Luca Tari, *Member, IEEE*, Gabriele Cavaliere, *Student Member, IEEE*, Sarah Sibilia, *Student Member, IEEE*, Antonio Maffucci, *Senior Member,IEEE* and Luigi Ferrigno, *Senior Member, IEEE*

***Abstract*—This work presents an innovative smart system for monitoring ice formation on photovoltaic systems (PV) based on capacitive sensors made of graphene nanoplatelet (GNP) nanocomposites and a low-cost conditioning circuit. At the heart of the methodological approach is integrating a multi-gap sensor configuration, designed to maximise sensitivity to dielectric variations, and an oscillator circuit that converts capacitance variations into frequency signals, ensuring robust and noise-free transmission even in extreme environments. The sensor design includes selecting innovative materials and an optimised electrode configuration. The metrological characterisation of the system shows a sensitivity down to almost 6 Hz/pF and a resolution of less than about 1.3 pF, confirming the system's excellent performance in variable environmental conditions and ensuring high accuracy in ice detection. Experimental tests with ice thicknesses of up to 10 mm showed perfect alignment with theoretical models. In addition, data analysis using machine learning techniques produced accurate results in classifying the presence of ice, with an accuracy of over 95% and remarkable robustness even in the presence of noise. The results confirm the system's high performance and versatility for PV, energy and aerospace applications, proposing a smart and energy-efficient solution for ice management in PV systems.**

***Index Terms*—Smart Monitoring, Smart Sensors, Smart Energy, Photovoltaic, Soiling, Conditioning System.**

I. Introduction

The economic viability of photovoltaic (PV) system deployment in polar and boreal regions—characterised by severe climatic conditions—has been previously demonstrated [1]–[3]. Despite the promising returns, these installations are significantly hindered by the accumulation of snow and ice, which adversely impacts both energy production and the structural integrity of the modules.

Structurally, snow and ice deposits exert additional mechanical loads on PV panels. If not adequately mitigated, such stresses may exceed design thresholds, leading to the formation of microcracks, corrosion of electrical connectors, surface degradation, and eventual delamination of encapsulant materials. From an energy perspective, snow and ice behave similarly to partial shading, hindering light transmission to the PV cells and resulting in a significant performance loss. It has been reported that energy losses in such conditions can reach up to 15% of the annual yield in snowy climates [1]–[3], representing a non-negligible cost.

Consequently, reliable monitoring and mitigation strategies for snow and ice are essential to ensure the long-term performance and profitability of PV systems in cold environments. Among the available techniques, heating-based de-icing solutions—particularly those leveraging the Joule effect—have shown effectiveness in removing ice. However, their continuous operation is energetically inefficient and economically unsustainable, particularly during periods of reduced solar irradiance. Therefore, a smart activation mechanism, guided by real-time ice detection, is required to optimise energy usage and reduce operating costs.

A wide range of ice detection methods has been investigated in the literature [4], [5], including ultrasonic [6]–[8], microwave [9], [10], infrared thermography [11], capacitive sensors [5], [12]–[14], and machine learning-based systems [15]–[17]. Although each approach offers specific advantages, many require complex instrumentation or entail high implementation costs, limiting their suitability for large-scale or distributed applications such as PV fields. Table I summarizes the main technologies, highlighting their strengths and weaknesses.

Recent efforts have turned to nanomaterial-based sensing technologies [18], [19], which offer the potential for enhanced sensitivity, miniaturisation, and lower cost. Among these, graphene nanoplatelets (GNPs) have emerged as a compelling option due to their excellent physical properties, coupled with the feasibility of industrial-scale production via methods such as wet-jet milling, microwave irradiation, and liquid-phase exfoliation [20]. Previous studies conducted by the authors have explored the electrothermal characteristics of GNP-based composites for heating applications [21] and for temperature sensing [22], and more recently, have demonstrated their utility in capacitive sensors for ice detection

This study introduces a novel GNP-based capacitive sensing system specifically developed for ice detection in PV applications. In order to analyze a realistic case study representative of a real-world application, commercial GNP material marketed by *Nanesa srl* company [23]. The sensing principle relies on the variation of the dielectric constant induced by the presence of ice, which leads to a measurable change in capacitance. To enhance accuracy and robustness under varying environmental

Manuscript received April 19, 2021; revised August 16, 2021.

Corresponding author: Luca Tari

Luca Tari, Gabriele Cavaliere, Sarah Sibilia, Antonio Maffucci and Luigi Ferrigno are with the Department of Electrical and Information Engineering, University of Cassino and Southern Lazio, Cassino, 03043 Italy (e-mail: luca.tari@unicas.it, gabriele.cavaliere@unicas.it, sarah.sibilia@unicas.it, maffucci@unicas.it, ferrigno@unicas.it)

Luca Tari, Gabriele Cavaliere, Sarah Sibilia and Antonio Maffucci are also with EUT+ Institute of Nanomaterials and Nanotechnologies (EUTINN), European University of Technology, European Union

Gabriele Cavaliere is also with Department of Information and Electrical Engineering and Applied Mathematics, University of Salerno, Fisciano, 84084, Italy, (email: gcavaliere@unisa.it)

conditions, the sensor adopts a multi-gap electrode configuration, optimised for improved metrological performance.

To facilitate cost-effective and scalable integration, the sensor is coupled to a custom-designed signal conditioning circuit. The choice of conditioning architecture was guided by physics-theoretical considerations underlying the operating principle while evaluating the metrological properties of different conditioning strategies. The most suitable approach was identified as a low-complexity circuit based on an oscillator, ensuring ease of implementation in real-world scenarios and scalability. This solution effectively translates capacitance variations into frequency variations, simplifying digital signal acquisition and processing. After selection, the conditioning circuit is designed, ensuring sensitivity and stability. The complete sensing system, including the acquisition part, was subsequently validated through experimental tests. Finally, the collected data were processed using machine learning techniques to define possible analysis methodologies aimed at detecting and estimating the amount of ice.

The proposed system is intended for distributed integration into PV arrays, enabling real-time, location-specific monitoring of ice formation. The proposed system can be directly integrated into PV panels or designed as a separate system as required. In both cases, this capability facilitates intelligent thermal management, whereby de-icing systems can be activated only upon verified ice presence, thus significantly improving energy efficiency and reducing operational expenditures. Although the focus is on PV systems, it is worth mentioning that the proposal is also an optimal solution for aerospace contexts, e.g. for ice detection on aircraft wings.

The paper is organised as follows: section II discusses the sensor fabrication methodology, the underlying sensing principle and the characterisation; section III and section IV present the analysis, design and implementation of the oscillator-based conditioning circuit, and the realisation and characterisation of the measurement system respectively. Finally, section V reports the results analysis and evaluates system performance, assessing the potential of the system with classification algorithms and section VI offers concluding remarks and perspectives for future research.

II. The novel graphene sensor

The sensor proposed in this work is configured as a planar capacitor, in which the electrodes are fabricated from a GNP-based composite processed into thin films and subsequently cut into strips. Figure 1 shows a schematic representation of the developed sensor. This configuration enables a non-invasive, lightweight architecture well-suited for integration on PV systems, where both sensing and actuation capabilities are desirable. The fringing electric fields at the strip edges were leveraged for design, enhancing sensitivity to dielectric changes in the surrounding environment. The rationale for selecting this nanocomposite material is twofold: it enables dual functionality—serving both as a capacitive sensing element and, potentially, as a Joule-heating actuator [24]—and it offers a significantly lower density than conventional metallic conductors, thus minimising added mass. In this work, only the sensing properties are considered.

TABLE I
A BRIEF OVERVIEW OF THE MAIN ICE-SENSING TECHNOLOGIES AND THEIR MAIN FEATURES. REPORTS THE ADVANTAGES AND LIMITATIONS FOR EACH TECHNOLOGY.

Technology	Advantages	Limitations
Ultrasonic [6]–[8]	Good SNR, suitable for metallic or composite structures	Point-based, sensitive to vibration and temperature
Microwave [9], [10]	High sensitivity, high selectivity	Requires calibration, higher cost, EM interference
Thermography [11]	Non-contact, large-area and real-time monitoring	Strongly affected by environment
Capacitive [**?**], [12]–[14]	Simple, low-cost, robust	Moderate sensitivity, influenced by humidity and temperature
ML-based [15]–[17]	High accuracy in classification and icing prediction	Large training datasets

A. Material Fabrication and Properties

The GNP-based electrodes utilised in this study are made of a paper-like industrial-grade material produced and marketed by the company *Nanesa srl* [23] with the commercial name "G-Preg 95/5", composed predominantly of graphene nanoplatelets (95%), with polyurethane (5%) employed as the polymeric binder.

The GNPs are obtained from a graphitic precursor via thermal expansion and a proprietary liquid-phase exfoliation technology. Their average lateral dimension is about 30µm, whereas the average thickness is 14 nm that corresponds to about 40 graphene layers, see [25]. The results of a morphological characterization made by using Scanning Electron Microscopy and Raman spectroscopy confirms the structural integrity of the graphene lattice and a very low presence of defects, as reported in [25]. The papers adopted in this work are fabricated starting from GNPs dispersed in solution, to which the polymer binder is added, with the scope of enhance the mechanical stability of the final film. The mixture is sprayed on a substrate by using a semiautomatic 3-axes pantograph (EXTREMA CNC, model Basic) and a spray nozzle (NCS, model full cone air nozzle). A cold calendaring at a controlled pressure up to 10 kN/m is then applied, followed by a final thermal annealing step, in order to enhance GNP alignment, reduce surface roughness, improve electrical conductivity, and stabilize the nanocomposite. Further details such as the results of the material characterization may be found in [25].

The GNP strips used in this work are 1 cm wide, 100 cm long, with an average thickness of 75 μm.

B. Sensor Architecture

The fabricated GNP strips are manually assembled onto an FR4 substrate in a coplanar configuration, forming the electrodes of the capacitive sensor. Three parallel electrodes are aligned at predefined distances to form two independent capacitive elements with differing geometries.

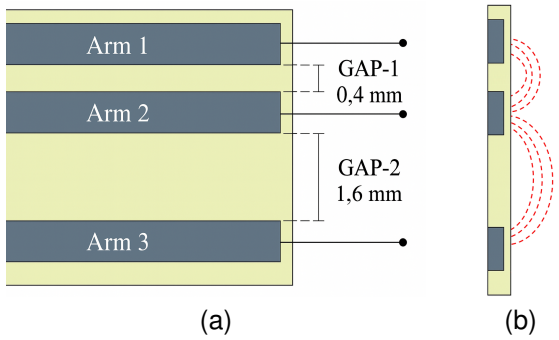

Fig. 1. Top view (a) and side view (b) of the conceptual schematic of the planar capacitor. The side view qualitatively shows (red dotted line) the electric field lines between the capacitor arms.

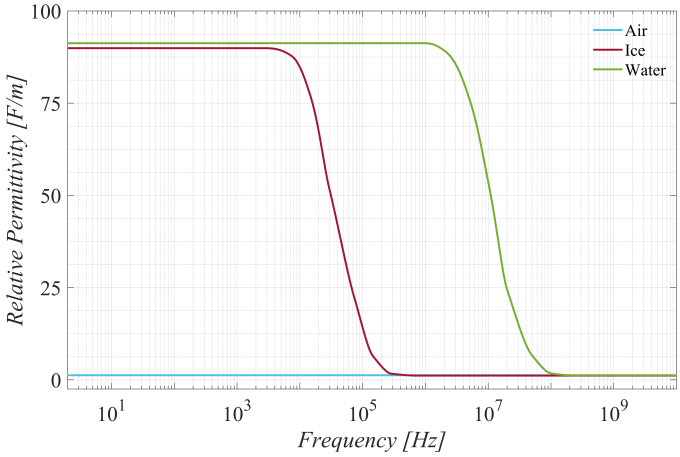

Fig. 2. Relative permittivity of distillate water and ice from distillate water with respect to air [30]. It shows the qualitative average behavior as frequency changes.

In particular, according to Figure 1:

- Capacitor 1: Formed between Arms 1 and 2, separated by a 0.4 mm gap, defined as GAP-1.
- Capacitor 2: Formed between Arms 2 and 3, with a 1.6 mm gap, defined as GAP-2.

To ensure environmental durability and prevent mechanical or chemical degradation, the entire sensor surface is laminated with a 25 μm thick Kapton film. This flexible, thermally stable polyimide layer provides electrical insulation without significantly altering the sensor's dielectric interface.

C. Operating Principle

Each pair of electrodes in the sensor forms a planar capacitor in which the total capacitance C_{Tot} can be modelled as the sum of two contributions:

$$C_{Tot} = C_{Bulk} + C_{Fringe} \tag{1}$$

where :

- C_{Bulk} : Arises from the field penetrating directly through the dielectric substrate; largely invariant to environmental changes.
- C_{Fringe} : Associated with fringing electric fields that extend beyond the electrode boundaries and are highly sensitive to the permittivity of the surrounding medium.

This edge effect enables the sensor to detect dielectric changes such as ice or water accretion, which exhibit permittivities orders of magnitude greater than air—particularly in the frequency range of interest. Figure 2 illustrates this difference, comparing the relative permittivity of air, ice, and liquid water as a function of frequency [26]–[29].

Reducing the electrode gap enhances the overall capacitance and the sensitivity of the device to small dielectric variations; however, it simultaneously reduces the penetration depth of the fringing electric field, which typically extends up to about four to five times the gap spacing [31]. Hence, an excessively narrow gap would improve sensitivity but lead to early saturation, limiting the ability to detect thicker ice layers. To empirically balance these effects, two geometries were adopted: GAP-1 (0.4 mm), optimised for high sensitivity and early detection of thin ice films, and GAP-2 (1.6 mm), designed to extend the sensing depth and maintain measurable response for thicker ice accumulations. This complementary configuration ensures good coverage of the ice growth range on photovoltaic surfaces.

D. Sensor Characterization

An initial characterisation was performed under controlled environmental conditions using an ACS DY110 climatic chamber to evaluate the sensor's behaviour and stability. Specifically, impedance measurements were conducted in the frequency domain employing a benchtop impedance analyzer (GW Instek LCR-8110G) in slow mode, interfaced with a PC via GPIB-488. Given the intrinsic properties of graphene-based sensors, the impedance of both GAP-1 and GAP-2 was modeled using a parallel R-C equivalent circuit.

To verify measurement repeatability, a series of 30 acquisitions was carried out using a four-wire configuration. Prior to data collection, the instrument was calibrated and capacitive shielding was implemented to minimize parasitic effects. The frequency range investigated spanned from 20 Hz to 100 kHz with logarithmic step increments.

Figure 3 presents the results of the characterisation of both GAPs under variable temperature (fixed humidity) and variable humidity (fixed temperature) conditions. For the sake of clarity, only the average capacitance response for each configuration is shown, as the dispersion between repeated measurements was negligible, due in part to the high metrological performance of the laboratory LCR meter. Specifically, the worst recorded standard deviations for the four tests shown in Figure 3 are: (a) 0.43 pF, (b) 0.37 pF, (c) 0.57 pF and (d) 0.56 pF. All of these values are obtained in correspondence of 20 Hz. Within the studied frequency range, both GAPs showed an almost flat behaviour, confirming their good frequency stability and the absence of significant dielectric dispersion effects in the operating region. A slight crossover between the capacitance curves at -20 °C and -40 °C can be observed in Figure 3.b at low frequencies, after which the values tend to converge at higher frequencies.

This phenomenon may be related not only to parasitic phenomena, but also to temperature- and residual moisture-dependent polarisation mechanisms and the polymer substrate, which slightly increases the effective permittivity at low frequencies.

Overall, capacitance variations with temperature and humidity remained below around 5 pF, confirming the robustness of the approaches. In detail, considering the entire frequency range examined, the average capacitance of GAP-1 is 51.17 pF with a standard deviation of 1.68 pF (3.29%), while GAP-2 shows 47.33 pF with a standard deviation of 0.58 pF (1.23%). The higher capacitance of GAP-1 results from the narrower spacing between the electrodes, which improves fringe-to-field coupling and reactivity to dielectric variations, in contrast for GAP-2. The recorded stability and complementary behaviours validate the hypothesised multi-gap design

III. Conditioning System Design

According to the operating principle described in the previous section, the information collected by the sensor (i.e., the presence of ice) is converted into a capacitance value. Consequently, this chapter first presents a theoretical estimation of the fringe capacitance and its dependence on ice accumulation.

Next, the conditioning methodology chosen for the sensor is presented. Various conditioning architectures were preliminarily evaluated in order to find a suitable compromise for the application. For the sake of brevity, only the final design of the selected conditioning circuit is discussed here, while a brief summary of alternative configurations is provided in Appendix (section VII).

A. Fringing Capacitance: Ice Dependence

This subsection presents a preliminary analysis to study the fringing capacitance and its dependence on ice accumulation. This investigation is essential for defining the expected order of magnitude of capacitive variations induced by environmental changes and for setting appropriate design constraints in the selection of the signal conditioning system.

Although various modelling approaches and correction theories have been proposed to increase estimation accuracy [32], for this study, it is possible to study fringing capacitance using the Palmer formula Equation 2. High precision estimation is not required at this stage; a coarse approximation is sufficient to define an operative design range.

The Palmer formula [33] for estimating the fringing capacitance of a planar capacitor is given by:

$$C_f = \frac{\varepsilon_r \varepsilon_0 W L}{G} \cdot \alpha_1 \alpha_2 \tag{2}$$

with the geometric factors α_1 and α_2 defined as:

$$\alpha_1 = 1 + \frac{G}{\pi W} + \frac{G}{\pi W} \ln\left(\frac{2\pi W}{G}\right) \tag{3}$$

$$\alpha_2 = 1 + \frac{G}{\pi L} + \frac{G}{\pi L} \ln\left(\frac{2\pi L}{G}\right) \tag{4}$$

where:

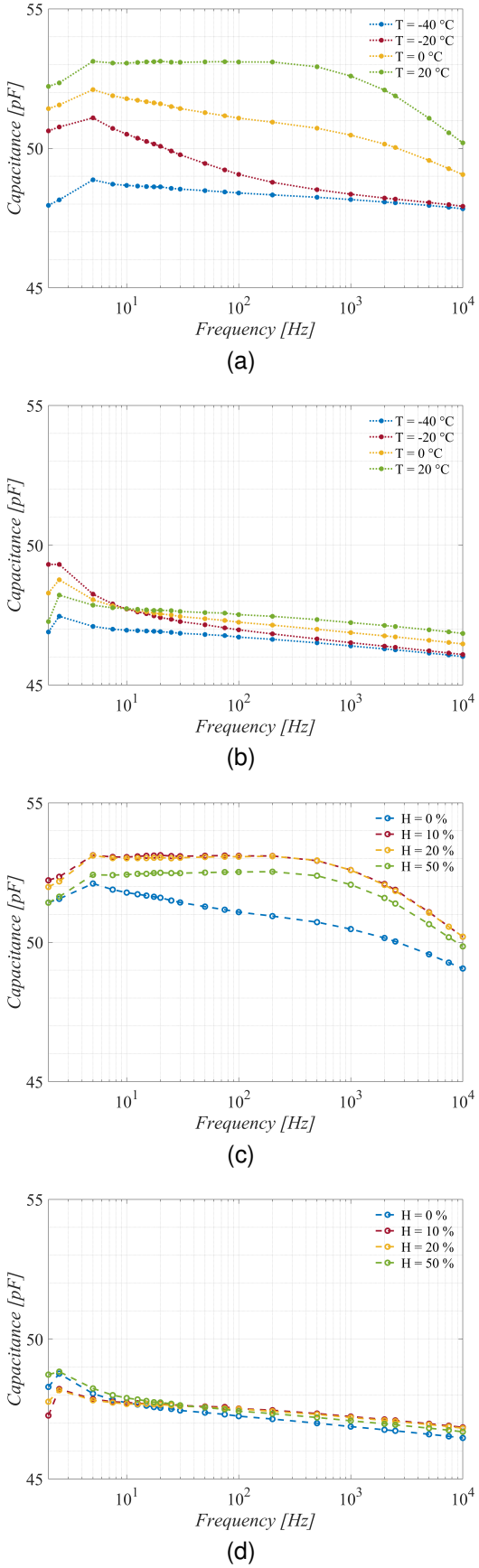

Fig. 3. Frequency variation of capacity versus environmental conditions (temperature and humidity varied individually). (a) and (b) show the characterisation under varying temperature and humidity for GAP-1, respectively; (c) and (d) show the characterisation under varying temperature and humidity for GAP-2, respectively.

- C_f: fringing capacitance;
- ε_r, ε_0: relative and vacuum permittivity, respectively;
- W: electrode width;
- L: electrode length;
- G: gap distance between electrodes.

From equation Equation 2, it is evident that fringing capacitance is highly sensitive to both geometric parameters and the dielectric constant of the surrounding material. In the context of this study, the sensor geometry remains fixed; therefore, the primary source of variability lies in the dielectric properties of the medium, specifically, ice. Accurately characterising the dielectric constant of ice is complex due to its dependence on multiple physical and environmental factors [34]. These include ice density (e.g., sea ice vs. distilled water ice), freezing temperature, ice morphology (e.g., compact vs. rime ice), crystal structure, water purity or presence of ions, and layer thickness. Furthermore, the dielectric permittivity of ice is known to vary significantly with frequency and temperature due to Debye relaxation mechanisms [35]. At low frequencies (typically below 10 kHz), the static dielectric constant ε_s dominates, whereas at higher frequencies, dispersion effects lead to a notable decrease in ε_r.

Given these challenges, a deterministic model of capacitance variation due to ice accretion is impractical for design purposes. For this reason, a conservative design assumption was adopted based on literature data and preliminary multiphysics simulations: the ice layer contributes approximately 5 pF/mm of additional capacitance. This figure aligns well with empirical data reported in recent studies on ice capacitance monitoring [36], [37]. In general, reported variations for ice layers of different thicknesses are consistently in the range of a few picofarads per millimetre, supporting the chosen assumption.

This preliminary value was further corroborated by COMSOL multiphysics simulations, confirming that a 1 mm thick ice layer yields a capacitance variation near pF sufficient for detection using the proposed sensing strategy. In detail, the model developed here is a simple 2D model. The two strips of graphene are placed on an insulation substrate about 3.5 mm thick. On the top of the strips, a Kapton layer (25-µm thickness) is interposed between the arms and an area 1 mm thick which represents both air or ice according to the considered operational conditions. The classic electrostatic problem is solved to derive the distribution of the electrical field, E, and the electric displacement field D, according to:

$$\nabla \cdot D = \rho \tag{5}$$

$$D = \varepsilon E \tag{6}$$

After solving the electrostatic problem, the bulk capacitance is extracted by calculating the electrical energy U stored in the whole solution domain, where three conductors are modelled: the two arms and a reference one, here represented as an external box far enough from the arms, whose electrical potential is set to zero. Three partial capacitances are associated with such a system: the capacitance between the two arms (C_{12}), and the capacitances between each arm and the reference conductor (C_{11} and C_{22}). Denoting with V_1 and V_2 the electrical potentials of the two arms with respect to the reference conductor, the total energy stored in the domain is expressed by:

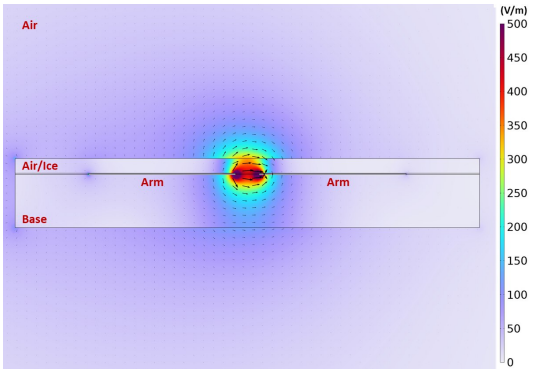

Fig. 4. Result obtained from the COMSOL simulation of the sensor GAP-2. It show: Electric field norm [V/m] by means of a colour map representation and electric field distribution by means of lines.

$$U = \frac{1}{2}C_{11}V_1^2 + \frac{1}{2}C_{22}V_2^2 + C_{12}V_1V_2 \tag{7}$$

It follows that the partial capacitance values in Equation 7 can be calculated by evaluating the energy associated with the following potential distributions:

$$\begin{cases} V_1 = 1, & V_2 = 0 \\ V_1 = 0, & V_2 = 1 \\ V_1 = 1, & V_2 = -1 \end{cases} \quad [V] \tag{8}$$

Finally, in order to obtain the capacitance value of the 3D structure, the result is multiplied by the length of the sensor. The simulation is performed in the presence of air upon the sensor and in the presence of 1 mm of ice. Figure 4 shows the output of the COMSOL simulation in the case of GAP-1 where the effect of the fringe field can be appreciated through a representation of the electric field lines and colour map. The calculated variation in capacity as a function of thickness obtained is par to 8.55 pF/mm for GAP-1 and 4.72 pF/mm for GAP-2. The values obtained are in agreement with the theoretical analysis discussed above.

B. Development of the Oscillator-Based Conditioning Circuit

The comparative analysis in Appendix (section VII) has shown that amplitude- or cutoff-frequency-based conditioning schemes, such as RC, RLC or bridge circuits, offer limited sensitivity, are strongly influenced by parasitic effects and are difficult to size for the capacitances in question. In contrast, the oscillator-based approach directly converts capacitance variations into frequency shifts, providing better noise immunity, stability and repeatability, which are critical from a metrological point of view.

The astable configuration with NE555 was therefore selected as the best compromise between stability, sensitivity and possible costs in terms of implementation, which is strategic for distributed ice monitoring applications.

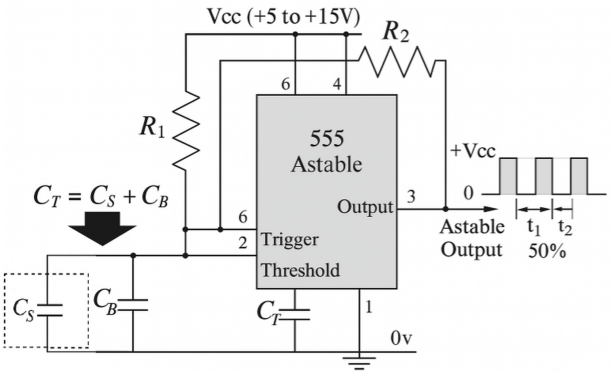

Fig. 5. Conditioning circuit based on NE555 oscillator. In detail: C_S represents the capacitive sensor, and C_B is the ballast capacitance for operating point selection. The dotted line around C_S indicates the shielding.

In particular, the selected conditioning architecture relies on a dedicated astable NE555 oscillator circuit for each GAP, which converts the measurement information (capacitance variation) into a frequency-modulated square-wave signal. The circuit topology is shown in Figure 5.

According to Equation 9, the total capacitance C_T charges and discharges through resistor R_2, resulting in a periodic output waveform with 50% duty cycle. The output frequency of the oscillator, being a direct function of C_T, in detail:

$$f = \frac{1}{0.693 \cdot 2R_2C_T} \tag{9}$$

with:

$$C_T = C_S + C_B \tag{10}$$

where:

- C_T: total capacitance;
- C_S: variable ice sensor capacitance;
- C_B: high accuracy fixed ballast capacitance.

The oscillator was carefully designed based on Figure 2, selecting an operating point within the frequency range where the dielectric constant of ice shows the strongest contrast with air, thus ensuring maximum sensitivity to dielectric variations. At the same time, a sufficiently high oscillation frequency was targeted to minimise the size of passive components and reduce noise susceptibility. A deliberate choice of 2 kHz for GAP-1 and 2.5 kHz for GAP-2 was made to both ensure clear signal separation between the two sensing elements and to remain within the optimal low-frequency region where the permittivity contrast between air and ice is most pronounced. These values were therefore not arbitrary but represent the best trade-off between sensitivity, stability, and component feasibility. Based on this operating point, the parameters C_B and R_2 were dimensioned accordingly to achieve the desired working conditions.

To ensure system stability, while retaining adequate sensitivity, C_B was set to 330 pF—sufficiently close in amplitude to the sensor capacitance (Figure 3) to avoid overwhelming the signal, yet large enough to stabilise the oscillator. The value of 330 pF was selected empirically from among available commercial capacitors.

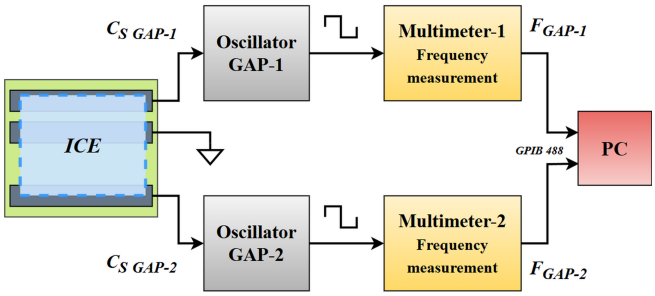

Fig. 6. Block diagram of the implemented measurement setup. The system receives the capacitance of the corresponding GAP as input to each oscillator, and produces a square-wave output whose frequency is subsequently measured by PC-controlled multimeters.

Subsequently, R_2 was selected to achieve the target frequencies, given a total capacitance $C_T \approx 380$ pF. To remain within the desired operating range (2–2.5 kHz), R_2 needed to fall within 500 kΩ–1 MΩ. Considering these constraints and commercial availability, the final selected values were 820 kΩ for GAP-1 and 680 kΩ for GAP-2, respectively. This configuration guarantees a robust, low-cost, and high-precision conditioning solution for distributed ice PV monitoring.

IV. Experimental Setup and Preliminary Results

This section presents and characterises the measurement setup, validates the proposed approach, and illustrates the experimental test setup conducted.

A. Experimental Measurement Setup

To power the two oscillator circuits, a laboratory-grade isolated dual-channel power supply (EL302RTAIM-TTI) was employed to eliminate unwanted coupling effects between the channels and to ensure electrical isolation across the measurement paths. Having established the operation of both the sensor and the conditioning system, the final element in the measurement chain consists of the instrumentation used to acquire the frequency of the square wave signals output by the oscillators corresponding to each GAP. In particular, each GAP - and thus each oscillator - was monitored with a precision multimeter (Agilent 34401A), configured in “High Resolution” mode, both and remotely controlled via the GPIB-488 interface.

Figure 6 illustrates the block diagram of the implemented setup, which summarises the whole measurement chain. Data acquisition and device control were done in the MATLAB environment via a dedicated PC. Figure 7 shows the experimental set-up realised and the various tools and equipment used to perform the tests.

B. Metrological Characterization of the conditioning system

At this stage of the work, a complete metrological characterisation of the overall system was carried out to evaluate the performance of the oscillator-based conditioning circuit described in the previous section.

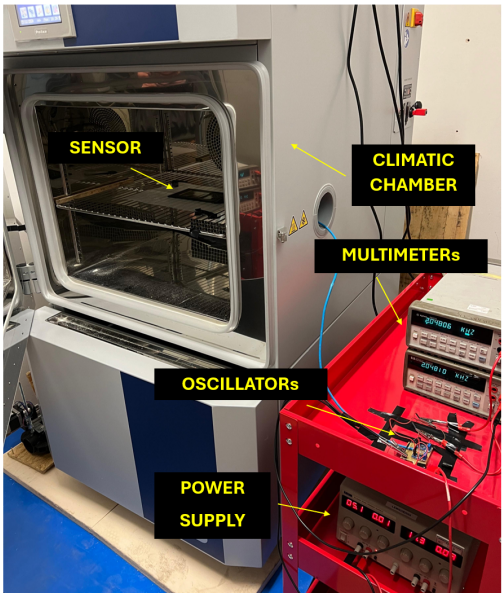

Fig. 7. Experimental setup realised to perform tests. It shows the different instruments and equipment adopted.

This phase aimed to assess the most relevant performance indicators—namely, linearity, sensitivity, and resolution—within a capacitance range compatible with the expected operating conditions of the sensor.

As the GNP-based sensor had already been characterised previously and given its stability, to avoid introducing uncontrolled variability during the test phase, the sensor (C_S) was replaced with a high-precision decade capacitor (QuadTech 1413). This configuration allowed a controlled and repeatable variation of the input capacitance, enabling a rigorous evaluation of the system's response regarding oscillation frequency. Of course, during the characterisation process, the fixed input values of the decade capacitor were measured with a precision LCR meter. This ensured that the acquired frequency data could be accurately correlated with the actual value of the applied capacitance. For each configuration tested, 20 frequency and capacitance measurements were recorded for each GAPs. This repeated acquisition allowed a more rigorous analysis.

1) Conditioning system linearity and sensitivity: To evaluate the global linearity of the system response, a nominal capacitance step of 50 pF was selected. Starting from a baseline value, the capacitance was increased in increments of 50 pF up to a total increment of 500 pF. The initial baseline capacitance included the 330 pF ballast capacitor (subsection III-B) and any systematic parasitic capacitances introduced by the measurement system and the connection cables. For each capacity step considered, 30 repeated measurements were performed to assess the dispersion of the data. The results of this analysis are presented in Figure 8.The uncertainty band of the fitted model (indicated by the dashed green lines) was automatically generated based on the dispersion of the measurements at each capacity step. The results obtained in this global sweep, shown in Figure 8a for GAP-2 (GAP-1 is similar minus a vertical shift), highlighted a clearly non-linear behaviour of the oscillator frequency response concerning capacitance. Among the models tested, the one that best minimised the Root Mean Squared Error (RMSE) was a fourth-order polynomial, which yielded an RMSE of approximately 70 Hz for each sensing channel (both GAPs). This non-linearity is not unexpected, given the non-linear dependence of frequency on the reciprocal of the total capacitance in the oscillator Equation 9.

However, considering the specific application context, the system is expected to operate in a small signal regime, where capacitance changes induced by ice layers occur in the order of a few picofarads (subsection III-A). Under these conditions, it is not necessary to maintain global linearity; instead, a local linearization of the response curve around the operating point is both appropriate and sufficient. To this end, a local linearization was carried out in the range 350 pF to 550 pF, which corresponds to the expected operational interval derived from the combined contribution of the ballast capacitor and typical sensor capacitance values (according to subsection II-A and Figure 3). Within this interval, a first-order model was fitted to the frequency data for each gap.

Two metrological parameters were extracted from this localised model:

1) The linearity, expressed as the RMSE of the first-order fit within the 350–550 pF range;
2) The sensitivity, defined as the slope (angular coefficient) of the linear model, in units of Hz/pF.

Figure 8b shows the zoomed-in region for GAP-2 used for the linearization and sensitivity estimation. Equivalent behaviour was observed for GAP-1, and thus, the methodology was consistently applied to both sensing channels.

2) Conditioning system resolution: To estimate the system resolution, a test was designed in which the capacitance was increased in five nominal steps of 1 pF starting from an initial capacitance value of 50 pF, added to the 330 pF ballast to obtain $C_T \approx 380$ pF. This reflects the realistic total capacitance expected during system operation (see subsection III-B). The choice of 1 pF as a step size was based on the minimum resolution achievable by the decade capacitor. For each step 30 repeated measurements was performed to asses the variability of the system.

Figure 9 shows the output of this characterisation. The frequency values measured for each tested capacitance are reported in terms of their mean and standard deviation, considering a 99.7% confidence level, which corresponds to a coverage factor of $k = 3$ under the assumption of a Gaussian distribution. The results show that the frequency ranges obtained are never compatible, demonstrating that for intervals of 1 pF, the system is able to detect frequency changes. Since the real steps applied may not precisely match 1 pF due to decade capacitor tolerance, the final resolution was calculated as the mean of the actual capacitance differences, as measured by the LCR meter over the five tested points.

The final values of the main metrological parameters—RMSE, sensitivity, and resolution—obtained from the characterisation of both GAPs are summarised in Table II. These parameters represent a comprehensive quantitative assessment of the performance of the system under small-signal operating conditions.

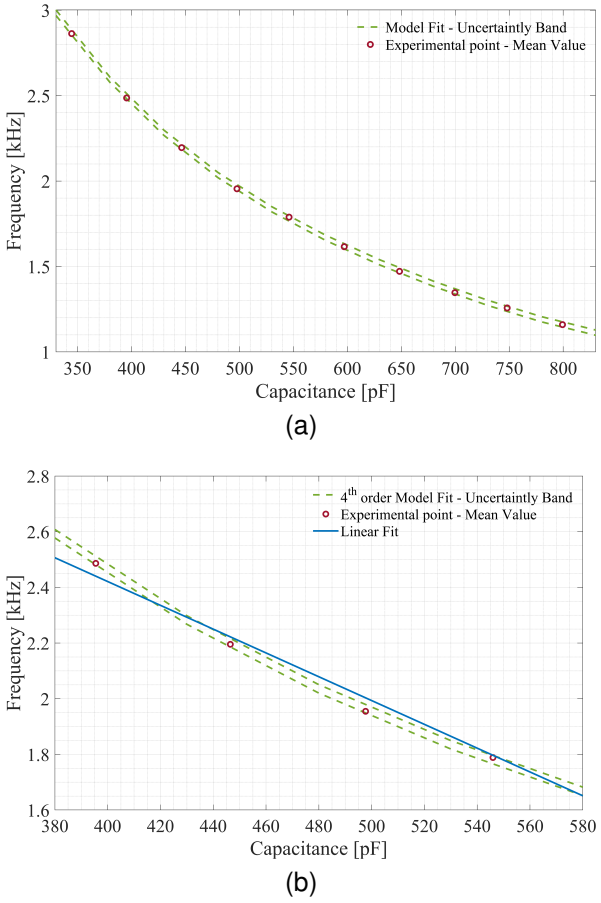

Fig. 8. Characterisation of system linearity and sensitivity. It shows: (a) Evolution of oscillator output frequency from GAP-2 as a capacitance function. (b) Zoomed-in view around the operating range to assess local linearity and extract sensitivity. The dashed green lines represent the uncertainty band of the fitted model, which was automatically derived based on the dispersion of the input measurements.

TABLE II
SUMMARY OF METROLOGICAL PARAMETERS EXTRACTED FROM THE SYSTEM CHARACTERISATION FOR EACH GAP.

Parameter	Conditioning GAP-1	Conditioning GAP-2
RMSE [Hz]	83.49	80.52
Sensitivity [Hz/pF]	5.67	4.95
Resolution [pF]	1.28	1.15

C. System Validation

Once the entire measurement setup was completed and verified, the metrological performances, a preliminary validation test was performed to confirm the correct functioning of the system as a whole. Specifically, according to the hypothesised operating principle, the objective was to verify whether the oscillation frequency output by the conditioning circuit varied in response to changes in the dielectric environment surrounding the sensor.

The test was conducted with the sensor placed inside a climatic chamber set at a stable temperature of $-20\,^{\circ}\mathrm{C}$. The overall duration of the test was 20 minutes, during which the output frequencies from both oscillators (corresponding to GAP-1 and GAP-2) were recorded at a fixed sampling interval of 4 seconds. During the initial 5 minutes, the sensor was monitored under baseline conditions with no external dielectric material applied. At the 5-minute mark, a controlled amount of demineralised water was carefully deposited onto the sensor surface using a custom-designed Kapton holder. Due to its dielectric neutrality and thermal stability, Kapton was explicitly selected to minimise the influence of parasitic or external capacitive effects. Approximately 20 mL of water was applied, corresponding to an estimated thickness of about 2 mm, given the holder's dimensions. Demineralised water was used to facilitate the test and better control the thickness, being identical to ice according to Figure 2.

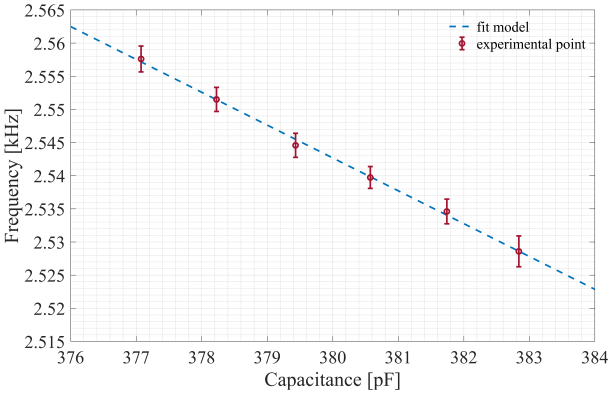

Fig. 9. Characterisation of system resolution. Frequency response of GAP-2 with nominal capacitance increments of 1 pF. The error bar represents the standard deviation of the input measurements.

TABLE III
BASELINE OPERATION OF THE MEASUREMENT SYSTEM. MEAN AND STANDARD DEVIATION OF THE OUTPUT OSCILLATION FREQUENCIES FOR EACH GAP, COMPUTED OVER THE FIRST 5 MINUTES OF THE TEST.

Baseline Frequency	GAP-1	GAP-2
Average [Hz]	2016.09	2514.21
Standard Deviation [Hz]	0.65	0.76

The results of this test are shown in Figure 10, in absolute terms and as a percentage change from baseline. The system demonstrates stable baseline behaviour in the first segment (0–5 minutes), with consistent oscillation frequencies and minimal standard deviation for both GAPs. These results confirm the system's robustness and absence of drift under constant environmental conditions. The average and standard deviation of the baseline frequency values during the first 5 minutes of acquisition are reported in Table III.

The observed difference between the two frequencies is entirely consistent with the sensor geometry and component sizing previously discussed in section II and subsection III-B.

Following the water deposition at minute 5, a clear decrease in frequency was observed for both GAPs, indicating a successful detection of the change in dielectric properties on the sensor surface. The variation was more pronounced in GAP-1, which—due to its narrower electrode spacing—is more sensitive to small changes in the effective dielectric constant and the proximity of the applied material.

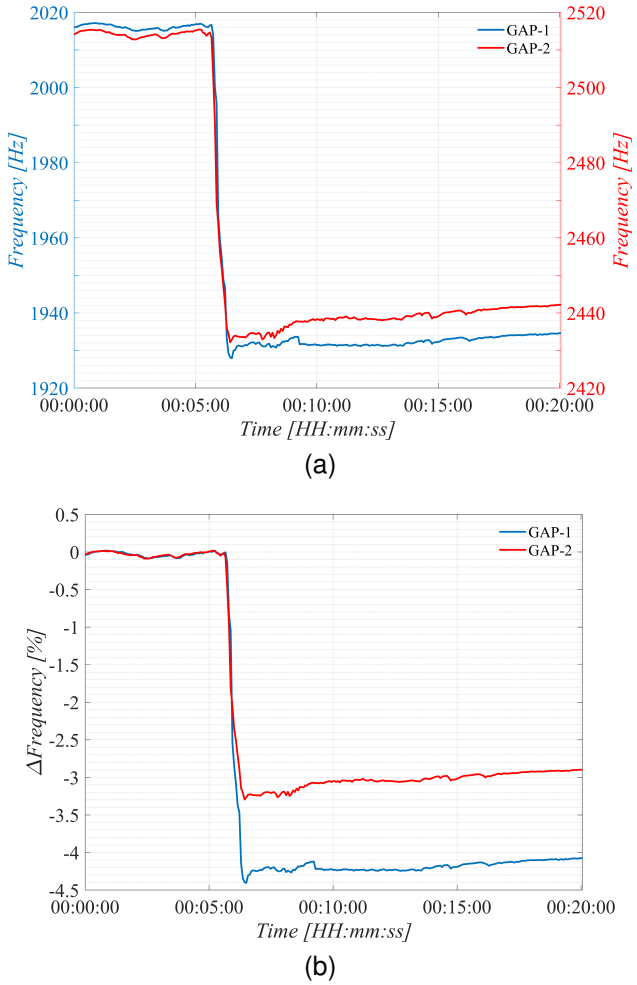

Fig. 10. Functional validation of the measurement system. (a) Temporal evolution of the oscillation frequency from GAP-1 and GAP-2 following the deposition of demineralised water. (b) Corresponding percentage variation relative to the initial baseline frequency.

This behaviour is consistent with the sensor architecture described in subsection II-B. It is worth noting that the test was conducted at $-20\,^{\circ}\mathrm{C}$, and only a small amount of water was applied. As such, the deposited water underwent complete solidification within 3 to 4 minutes after application. Interestingly, after the initial drop in frequency caused by the presence of liquid water, no significant further variation was observed during the subsequent minutes. This is an important observation, as it confirms the prediction illustrated in Figure 2: at the test frequency range (2–2.5 kHz), the dielectric constants of ice and water are sufficiently close that no significant shift in sensor capacitance occurs upon freezing. The sensor thus behaves similarly in the presence of either phase under these conditions, as anticipated by the theoretical model. This validation experiment confirms that the system: Responds correctly to changes in the surrounding dielectric medium; Exhibits excellent frequency stability under static conditions; Behaves consistently with theoretical expectations regarding permittivity transitions from air $\rightarrow$ water $\rightarrow$ ice. Overall, the results validate the correct functional integration of the sensing and conditioning system, thereby confirming its readiness for further specific tests.

V. Experimental Test and Analysis Results

In this section, experimental results are presented and an analysis based on a machine-learning approach is proposed for the detection and quantification of ice.

A. Test Configuration

The experimental tests in this section aim to test the system in the presence of different thicknesses and evaluate the related performance. It is important to note that demineralised water was used instead of ice to improve control over the target thicknesses. This substitution is justified according to the considerations made in the previous section. Furthermore, from the point of view of the assumed PV application, liquid water is unlikely to accumulate on the PV panel surfaces due to the inclination of the panels. The thicknesses examined were 2.5, 5.0, 7.5, and 10.0 mm. Based on the geometric configuration of the Kapton substrate, each stage of the testing procedure involved approximately 23 ml of demineralised water. The experimental protocol, conducted using the previously described setup, consisted of the following steps:

- Total test duration: approximately 10 minutes.
- Sampling interval: every 4 seconds.
- For the first 5 minutes, baseline measurements were recorded.
- At minute 5, a volume of water corresponding to the target thickness was added to the Kapton substrate.

B. Results

The results obtained with the test procedure described above are presented here. Frequency variations were recorded for each GAP. Figure 11 illustrates the oscillation frequency responses of GAP-1 and GAP-2 as a function of time and thickness in absolute terms and as a percentage change. Specifically, the results are presented in absolute terms and as a percentage change from the corresponding baseline. To facilitate the interpretation of the results, the reactions of each GAP to the different thicknesses tested are presented in a single figure with different colours. It is evident from the graphs that the frequency decreases as the thickness of the water, and thus the ice, increases.

This phenomenon is explained by the fundamental physics of capacitive sensors: when a medium with higher relative permittivity (e.g., water or ice) replaces air above the sensor, a larger number of electric field lines are confined within the dielectric due to fringing effects. Consequently, the effective capacitance of the sensor increases, leading to a decrease in the oscillator's output frequency.

However, the fringing field is spatially constrained. As noted in Section II-C, electric field lines close within a distance approximately 4–5 times the separation between the capacitor plates. Considering the width of the individual armature, for GAP-1, this distance is approximately [5.6-7] mm, while for GAP-2, it is approximately [9.6-12] mm. By this, the results in Figure 11a shows that GAP-1 becomes saturated at 7.5 mm and 10 mm thicknesses, indicating a reduced ability to discern further increases.

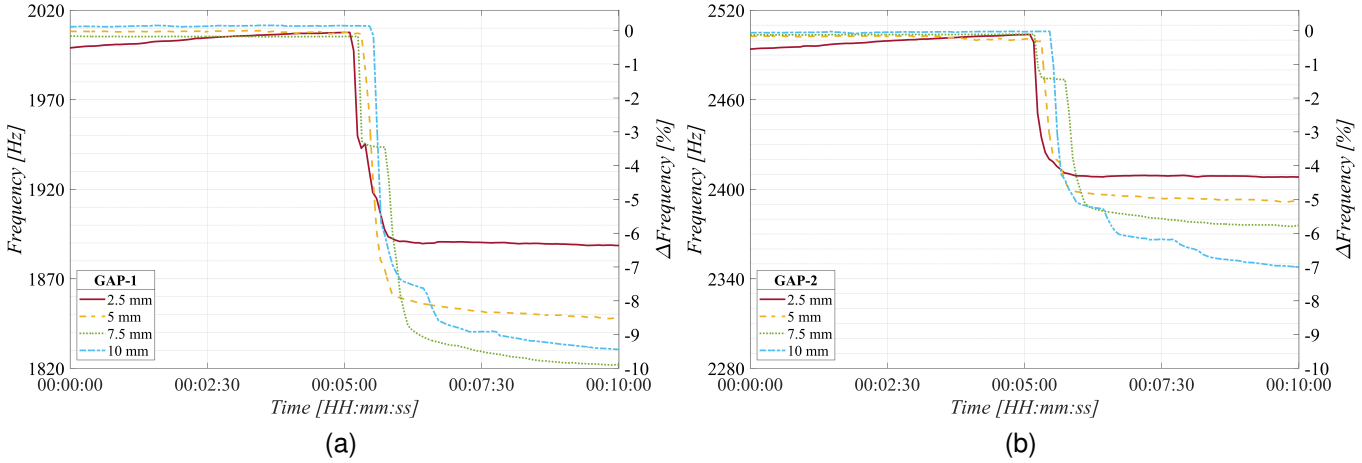

Fig. 11. Trend of the frequency emitted by the GAP-1 (a) and GAP-2 (b) oscillators for each thickness tested. Shows absolute responses (left axis) and responses in terms of percentage change in frequency from the corresponding baseline (right axis), averaged over the first 5 minutes.

GAP-1 exhibits high sensitivity at smaller thicknesses but a limited range. Conversely, looking at the responses in 11b, GAP-2 provides a progressive frequency variation as thickness increases but with less sensitivity at smaller thicknesses.

C. Comparison between theoretical and experimental "Frequency-Capacity" models

To analyse the performance of the system, further tests were conducted using an LCR meter to directly measure the capacitance offered by each GAP, considering the different thicknesses. The conditioning circuits were excluded from this phase. Following the test configuration and considering the frequency values recorded in the previous tests (subsection V-A), the frequency range analysed with the LCR meter was 1-3 kHz, with a step of 200 Hz. For each frequency, 10 repeated measurements were performed. Subsequently, the average capacitance values provided by the GAPs were calculated for each ice thickness within the analyzed range.

Figure 12 shows the results of this test, while Table IV summarises the obtained values. The corresponding standard deviation is also reported to provide an indication of the input measurements variability within the all considered frequencies range. From the table, the capacity variation offered is evident from the assumed operating principle.

Furthermore, in agreement with Figure 11, GAP-1 presents a "saturation" of its behaviour for thicknesses greater than 5 mm, but with greater sensitivity for smaller thicknesses. On the contrary, GAP-2 presents a progressive increase in capacity as thickness increases. Finally, according to subsection III-B, considering these capacitance values offered by the sensor C_S for each GAP and the values of C_B and R_2 chosen at the design stage, the corresponding theoretical frequency values were calculated, according to Equation 1. These theoretical values were compared with those obtained experimentally in subsection V-A, estimated as the average of the last 2:30 minutes of each test in Figure 11.

Figure 13 shows this comparison, from which it is possible to observe the good linearity of the experimental trends, in

TABLE IV
CAPACITANCE VALUES OF EACH GAP MEASURED EXPERIMENTALLY BY LCR METER, CORRESPONDING TO THE DIFFERENT THICKNESSES CONSIDERED. THE AVERAGE AND STANDARD DEVIATION ARE REPORTED OVER THE ANALYZED FREQUENCY RANGE OF 1–3 KHZ.

Thickness [mm]	**0**	**2.5**	**5**	**7.5**	**10**
GAP-1					
Average [pF]	54.37	68.49	71.83	74.05	74.37
Dev. Std. [pF]	0.17	0.18	0.19	0.20	0.19
GAP-2					
Average [pF]	50.56	62.04	66.11	67.74	69.97
Dev. Std. [pF]	0.27	0.23	0.16	0.18	0.25

agreement with the theoretical ones, except for the "saturation" of GAP-1 for the reasons described above (justifying the partial linearisation of the conditioning circuit response). The slope of the experimental curves depends, in agreement with subsection II-C, on the sensitivity of the GAPs, specifically being greater for GAP-1 as a smaller distance between the armatures characterises it. The theoretical and experimental trends agree, with the observed deviations primarily attributed to parasitic capacitances (hence to C_T according to subsection III-B), which introduce systematic offsets. A pseudo-linear trend of GAPs in different thickness ranges is evident from the results obtained. Given these characteristics, two separate linear models could be constructed: one for each sensor within its optimal range, defined up to 5 mm for GAP-1 and up to 10 mm for GAP-2.

D. A preliminary ice thickness classification based on ML approach

The aim of this section is to provide a preliminary analysis about the classification capability of the proposed sensor based on ML approach [38]. Certainly, for greater robustness and consistency of the analysis, more data should be considered. Therefore, the authors hereafter limit themselves to presenting

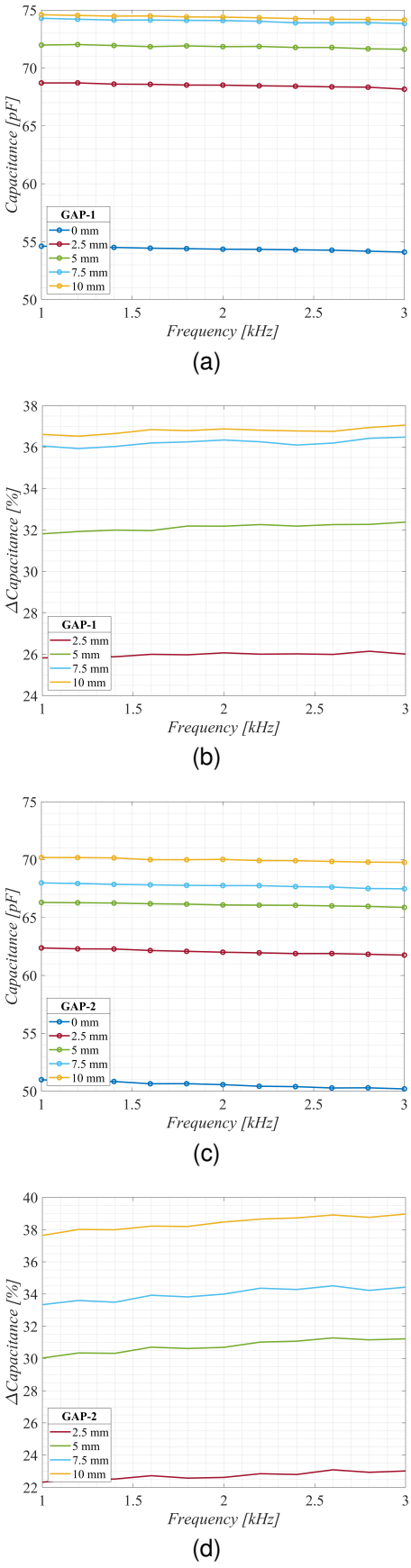

Fig. 12. Capacitance characterisation with LCR meter with different ice thickness. It shows in the 1-3 kHz of interval: (a) the measured capacitance and (b) the variation of capacitance concerning no ice presence for GAP-1; (c) the measured capacitance and (d) the variation of capacitance concerning no ice presence for GAP-2.

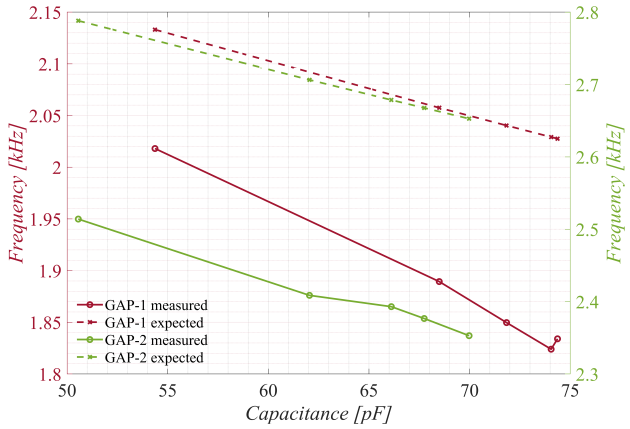

Fig. 13. Comparison between theoretical "Frequency-Capacity" curves (dashed lines) and those obtained experimentally (solid lines). The discrepancy can be attributed to parasitic effects and non-ideality of the real system.

a possible ML-based methodology that can certainly be optimised in future research aimed at increasing the TRL of the overall system. Considering the outputs of GAP-1 and GAP-2 as input features, a combined classification model is trained to account for these features simultaneously, allowing for joint processing, aimed at ice detection and quantification.

In particular, two classification scenarios were considered:

1) a binary classification (presence vs. absence of ice)
2) a multiclass classification (five distinct classes corresponding to different ice thicknesses, including 0 mm for the no-ice condition).

To this end, various machine learning algorithms were assessed using MATLAB's Classification Learner Toolbox. The Weighted k-Nearest Neighbors (Weighted k-NN) algorithm yielded the highest classification accuracy among the tested models. In brief, the k-Nearest Neighbors (k-NN) algorithm is a widely adopted supervised learning technique known for its conceptual simplicity and effectiveness in classification tasks [39]. For the binary classification task, each test was divided into two equal balanced segments: the first 5 minutes were labelled as the no ice class (Class 1), and the subsequent 5 minutes as the ice class (Class 2), corresponding to the different thicknesses tested.

Considering the measurement time, this procedure yielded 73 samples per class per test, resulting in a balanced dataset. In the multiclass classification scenario, five classes were considered: Class 1 representing no ice (0 mm), and Classes 2 to 5 corresponding to increasing levels of ice thickness. To maintain class balance, 73 representative samples were randomly selected for the no ice class from the first 5 minutes of the 4 available tests, while 73 samples for each of the remaining classes were obtained from the final 5' of all tests. The dataset was divided into training (80%) and testing (20%) for both classification tasks. Within the training set, 5-fold cross-validation was applied, using 5% of the training data in each fold to assess model generalisation performance. For the analysis, an additional feature was introduced to improve the performance of the model. In detail, the normalised frequency is defined as:

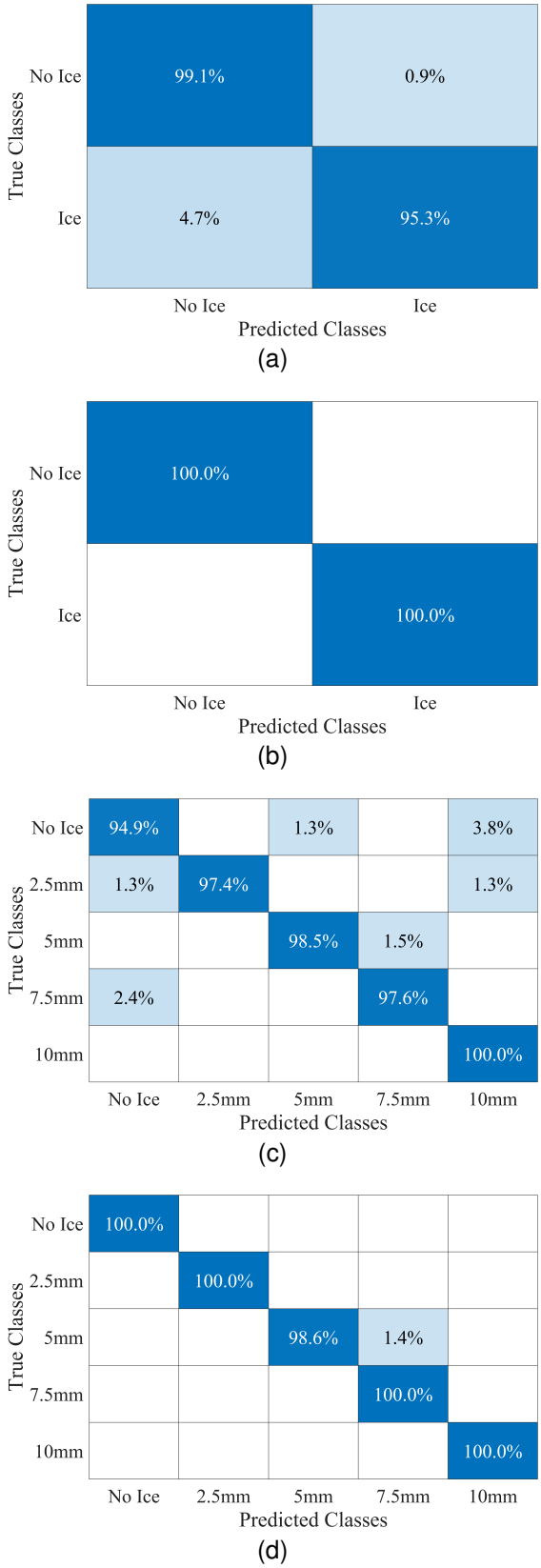

Fig. 14. Results obtained from machine learning-based analysis. It shows: results of binary classification (presence vs. absence of ice) considering two (a) and four (b) features as input to the model; results of multiclass classification (five distinct classes corresponding to different ice thicknesses including 0 mm) considering two (c) and four (d) features as input to the model.

$$f_{norm}[\%] = \frac{(f_{meas} - f_{baseline})}{f_{baseline}} \cdot 100 \tag{11}$$

where:

- f_{norm} is the normalized oscillator frequency;
- f_{meas} is the instantaneous measured oscillator frequency;
- $f_{baseline}$ is the average baseline frequency measured during the first 5 minutes.

Finally, to analyse performance as the size of the analysis feature space varied, the models were trained using two configurations:

1) two features (absolute frequency from each GAP);
2) four features (absolute and normalised frequency for each GAP).

Results in Figure 14 highlight:

- High classification accuracy for both detection and quantification tasks;
- Better performance in detection over quantification;
- Increased accuracy with the inclusion of the new defined normalised features.

Following the initial performance assessment, the system's robustness was evaluated by artificially adding Gaussian noise with zero mean and varying amplitude. This test was conducted for the four-feature case as input to the model. The noise levels were defined as multiples of the baseline standard deviation (σ), calculated over the first 5 minutes. Specifically, the amplitude tested were 2σ, 5σ, 10σ, and 15σ. This approach simulates realistic disturbances in the dynamic behaviour of the sensor output in the presence of ice that might occur under real conditions.

The results in Figure 15 confirm the effectiveness of the proposed classification framework, particularly for the no ice class, which remains correctly identified even under increasing noise levels. As expected, higher noise amplitudes lead to a gradual decrease in overall accuracy, more evident for thicker ice layers. Nevertheless, the majority voting strategy allows the correct class to remain dominant across all scenarios. Even under the most severe noise condition (15σ), all classes retain accuracies above 70%, except for the 10 mm case—previously identified as critical—which still achieves correct predictions in more than 60% of instances. This outcome reflects both the reduced sensitivity of the sensor near the upper limit of its measurement range and the limited amount of available data. Overall, the results demonstrate that the proposed methodology can reliably handle noise conditions, confirming its potential for robust ice detection and quantification.

Moreover, these results should be considered as preliminary feasibility tests rather than a fully generalised model. Further validation on larger and more diverse datasets will be necessary to consolidate the reliability of the proposed approach. Studies with a larger dataset will further consolidate these results and improve the consistency of the proposed analysis. For the sake of completeness, the ROC (Receiver Operating Characteristic) curve is reported in Figure 16 and shows, as for an example, the characteristics of the confusion matrix obtained in the worst condition at 15σ (Figure 15d).

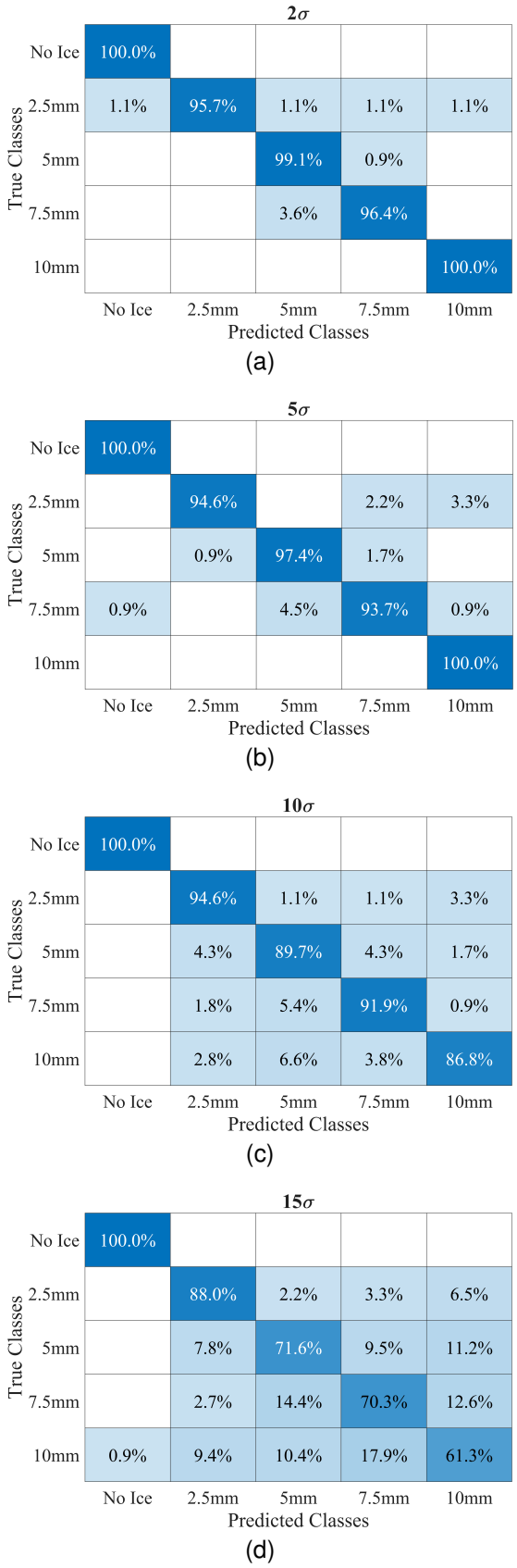

Fig. 15. Results obtained in the presence of different noise levels. Multiclass classification results with ice thicknesses: (a) 2σ, (b) 5σ, (c) 10σ, (d) 15σ.

The ROC curve shows good overall performance of the Weighted k-NN classifier, with high True Positive Rate (TPR) values for low False Positive Rate (FPR), especially for the "No Ice" and "2.5 mm" classes. A progressive degradation in discrimination is observed for higher ice thicknesses (7.5 mm and 10 mm), whose curves appear less pronounced, indicating a reduced ability to separate classes. However, considering the Area Under the Curve (AUC) values reported along the diagonal in Figure 15.d, the majority voting approach remains applicable for the final classification, confirming the robustness of the system even under the severe noise conditions.

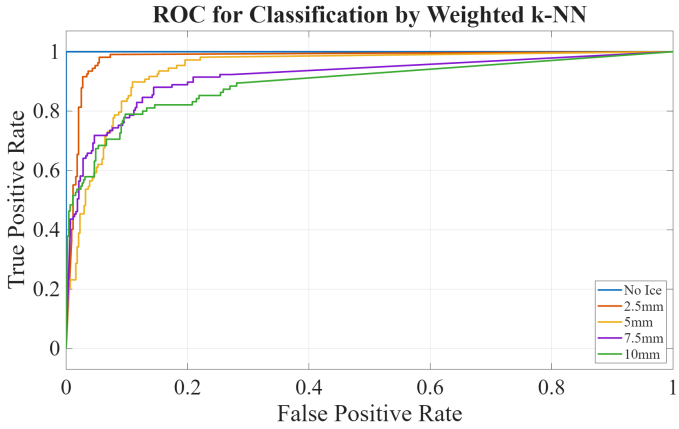

Fig. 16. Receiver Operating Characteristic (ROC curve) obtained in the worst noise condition 15σ (Figure 15.d).

VI. Conclusions

The work presented an innovative and methodologically sound approach for monitoring ice formation using capacitive sensors based on graphene-based nanocomposites, integrated with a robust and scalable conditioning system. The entire process, from design to realisation and characterisation, was guided by careful theoretical and experimental analysis, with the aim of achieving metrological performance and efficient implementation in real-world contexts.

The choice of a multi-gap architecture made it possible to optimise the system's response for different ice thicknesses. At the same time, adopting an oscillator circuit based on NE555 ensured excellent immunity to noise and a direct transduction from capacitive to frequency variations, favouring integration in distributed networks. In addition, the goodness of the associated metrological characteristics should be highlighted: resolution ($\approx 1pF$), sensitivity ($\approx 5-6Hz/pF$) and stability (standard deviation $< 1Hz$) emerged during characterisation.

Based on these obtained values, the system demonstrates an ice thickness resolution of around 0.2-0.3 mm, with a detection range from thin layers (≈0.2 mm) up to at least 10 mm (maximum value tested), depending on the geometry. Specifically, GAP-1 shows higher sensitivity for early ice formation, while GAP-2 maintains a measurable response for thicker accumulations, avoiding marginal field saturation. This complementary behaviour ensures accurate monitoring across the range of ice conditions expected in photovoltaic applications.

The experimental validation confirmed the theoretical predictions regarding the dielectric behaviour of water and ice in the operating frequency range, emphasising the effectiveness of the system in detecting the presence of ice through measurable capacitive variations.

Furthermore, the machine-learning-based analysis demonstrated the high accuracy of the system for both the detection of the presence of ice (binary classification) and its quantification (multiclass classification). As the results show, this is also the case in scenarios with noise, similar to real-life conditions.

A distinctive element of the present work is the rigorous methodological approach adopted in designing and evaluating the entire measurement system.

This approach has led to the development of a high-performance, replicable, and scalable solution. The proposed methodology is, in fact, transferable to numerous other application contexts, particularly in the aerospace sector for ice detection on critical aircraft surfaces, where it is essential to guarantee reliability, lightness and immunity to communication disturbances.

Among the most promising future prospects is the integration of water-ice discrimination techniques, exploiting a dual-frequency readout for each sensor GAP. This strategy could allow a more detailed analysis, distinguishing water and ice based on their different dielectric behaviour at selected frequencies. In addition, developments are planned in the area of sensor geometric optimisation, miniaturisation of the conditioning system and development of an ad-hoc, low-cost frequency measurement system. Further analyses will focus on validation in complex operating environments, including full-scale tests, considering different types of ice.

VII. APPENDIX

Preliminary Analysis of Conditioning Circuits

In order to identify the most suitable conditioning approach for the application at hand, a preliminary comparative analysis of different circuit topologies was performed. The objective was to evaluate their behaviour in response to small capacity variations and to determine the most robust and scalable solution for distributed sensing applications. Naturally, given the cost, direct measurement methods e.g. based on LCR meters or impedance spectroscopy [40] were excluded from the analysis.

Considering the sensor's baseline capacitance (Figure 3) and the expected variation range outlined in subsection III-A (around 5 pF/mm), it becomes evident that implementing a distributed measurement system—such as for monitoring ice accumulation on photovoltaic arrays—cannot rely on the transmission of raw analog signals due to parasitic effects. These effects would significantly degrade signal integrity over long distances. A viable alternative is to perform signal conditioning locally at each sensor node, converting the analogue variation into a more robust format (e.g., frequency, voltage amplitude or digital signal) before transmission.

To this end, preliminary simulation tests were conducted to compare various conditioning circuit topologies to evaluate their response to a nominal 5 pF capacitance variation. The following configurations were analysed:

- First-order RC low-pass filter;
- Second-order RLC band-pass filter;
- De Sauty bridge;
- Oscillator-based circuit.

1) First-Order RC Filter: In the case of the first-order RC low-pass filter, capacitance can be inferred by analysing the gain—defined as the ratio between output and input voltage (V_{out}/V_{in})—across the frequency domain. The transfer function is given by:

$$\frac{V_{out}}{V_{in}} = \frac{1}{\sqrt{1+\omega^2 R^2 C^2}} \tag{12}$$

However, to maximise sensitivity to small variations (of the order of 5 pF), the circuit must operate with a cutoff frequency ideally around 2 kHz, as suggested by Figure 2. Achieving this condition requires resistor values on the order of MΩ (e.g. 1.5 MΩ for a cutoff at 2.5 kHz), which are impractical in real low-noise systems. The addition of a high accuracy ballast capacitance can reduce R. To get an idea, with 300 pF of ballast, an R equal to 200 kΩ is obtained; under this condition, considering variations of 5 pF, the responses highlights a theoretical sensitivity of approximately -10 mV/pF. For this conditioning, the measurement of capacitance from a metrological point of view is indirect and subject to uncertainties in estimating the cutoff frequency and the measurement of input and output voltage. Therefore, these metrological characteristics make the circuit impractical due to susceptibility to noise and low dynamic performance.

2) Second-Order RLC Band-Pass Filter: Similar considerations apply to the second-order RLC band-pass filter. Capacitance can be estimated by locating the filter's resonance frequency, which is determined by:

$$f_r = \frac{1}{2\pi\sqrt{LC}} \tag{13}$$

Considerable resistance and inductance values are required to achieve a resonant frequency near 2.5 kHz. For instance, with $C = 50pF$, the corresponding inductance must reach approximately 80 H. This component value is unfeasible. To reach feasible values would require a relatively large ballast capacitance relative to the sensor. However, the simulated sensitivity data were carried out with the unfeasible inductance.

3) De Sauty Bridge: The De Sauty bridge is a classical AC method for measuring unknown capacitance values by balancing a bridge containing capacitive and resistive elements. The unknown capacitance C_x is obtained by:

$$C_x = C_1 \cdot \frac{R_1}{R_2} \tag{14}$$

However, this formulation assumes perfect balance and a zero-voltage detection instrumentation, which does not guarantee scalability and consistency for such applications. Alternatively, small variations in capacitance can be detected from the output voltage without rebalancing the bridge:

$$\frac{V_{out}}{V_{in}} = \frac{\omega R \Delta C}{1+(\omega R C_0)^2} \tag{15}$$

Even under idealised conditions, assuming R = 10 kΩ and a working point at 2.5 kHz and considering the capacitance variations in question, a sensitivity of 0.1 mV/pF is obtained. Nevertheless, this method requires near-perfect initial matching of the bridge capacitors, which is unfeasible given the material tolerances of the GNP-based sensors. Additionally, the accuracy depends strongly on the resistances accuracy.

4) Oscillator-Based Circuit: Belonging to the multivibrator family, they are circuits that oscillate between two logical states and are divided into three main types: astable, monostable and bistable. The astable multivibrator is a periodic signal generator that does not require an external trigger. Its frequency is determined by the time constant RC, and depends directly on the capacitance [41]. The monostable has a stable and a quasi-stable state: when it receives a pulse, it generates a temporary output, but does not produce continuous oscillations. On the other hand, the bistable has two stable states and remains in one of these until it receives an external input, without generating periodic signals. Of the three, the astable stands out for its ability to produce stable oscillations, making it ideal for capacitive measurement applications, ensuring a very robust transduction of information and suitable for the application in question (the information is associated with a frequency measurement). In detail, the frequency is directly related to the capacitance of the sensor according to:

$$f = \frac{1}{0.693 \cdot 2RC} \tag{16}$$

As an illustrative example, achieving an oscillation frequency of 2.5 kHz with a sensor capacitance of 50 pF would require extremely high resistance values—on the order of MΩ. Similar to the considerations for RC filters, a ballast capacitance can be introduced to stabilise the system. For instance, incorporating a 300 pF ballast capacitance allows for operation around 2 kHz with a resistance of approximately 800 kΩ. Under these conditions, given the assumed capacitance variation, a sensitivity of approximately -7 Hz/pF is obtained, which is very interesting from a design point of view.

As mentioned before, the advantage of this conditioning solution lies in the fact that the information is associated with a frequency, facilitating the measurement and transmission of information by being more immune to disturbances. These advantages, combined with the simplicity of the circuit, make oscillator-based conditioning a compelling choice for distributed capacitive sensing applications in harsh environments such as photovoltaics.

Table V summarises the sensitivity comparison for the evaluated signal conditioning circuits. From the considerations made, it is evident that the oscillator-based circuit shows the best characteristics for the assumed application. The excellent sensitivity shown simplifies and reduces the cost of measurement instrumentation, increasing immunity to disturbances. This system is also relatively simple to design and implement, with no significant problems expected in field applications, especially when a ballast capacitance is used, which does not significantly affect the overall performance of the circuit. Therefore, the astable oscillator-based approach was selected based on these comparative results.

TABLE V
COMPARISON OF ESTIMATED SENSITIVITY TO VARYING ICE THICKNESS FOR THE CAPACITIVE CONDITIONING CIRCUITS EVALUATED.

Conditioning Circuit	**Sensitivity**	**Feasibility**
First-order RC filter	-10 mV/pF	Limited
Second-order RLC filter	—	not feasible
De Sauty bridge	0.1 mV/pF	Sensitive to mismatch
Oscillator-based (astable)	-7 Hz/pF	Preferred

ACKNOWLEDGMENTS

This work was supported in part by the Project ECS 0000024 “Ecosistema dell’innovazione - Rome Technopole” financed by EU in NextGenerationEU plan through MUR Decree n. 1051 23.06.2022 PNRR Missione 4 Componente 2 Investimento 1.5 - CUP H33C22000420001. The Authors acknowledge the company Nanesa srl (Italy) for providing the GNP-based electrodes used in this work.

REFERENCES

[1] E. Andenæs, B. P. Jelle, K. Ramlo, T. Kolås, J. Selj, and S. E. Foss, “The influence of snow and ice coverage on the energy generation from photovoltaic solar cells,” *Solar Energy*, vol. 159, pp. 318–328, 2018.
[2] B. P. Jelle, “The challenge of removing snow downfall on photovoltaic solar cell roofs in order to maximize solar energy efficiency—research opportunities for the future,” *Energy and Buildings*, vol. 67, pp. 334–351, 2013.
[3] P.-O. A. Borrebæk, B. P. Jelle, and Z. Zhang, “Avoiding snow and ice accretion on building integrated photovoltaics–challenges, strategies, and opportunities,” *Solar energy materials and solar cells*, vol. 206, p. 110306, 2020.
[4] K. Wei, Y. Yang, H. Zuo, and D. Zhong, “A review on ice detection technology and ice elimination technology for wind turbine,” *Wind Energy*, vol. 23, no. 3, pp. 433–457, 2020.
[5] U. N. Mughal, M. S. Virk, and M. Y. Mustafa, “State of the art review of atmospheric icing sensors,” *Sensors & Transducers*, vol. 198, no. 3, p. 2, 2016.
[6] L. Yang, J. Chen, Y. Hao, L. Li, X. Lin, L. Yu, Y. Li, and Z. Yuan, “Experimental study on ultrasonic detection method of ice thickness for 10 kv overhead transmission lines,” *IEEE Transactions on Instrumentation and Measurement*, vol. 72, pp. 1–10, 2023.
[7] V. Carlsson, “Measuring routines of ice accretion for wind turbine applications: The correlation of production losses and detection of ice,” 2010.
[8] P. Wang, W. Zhou, Y. Bao, and H. Li, “Ice monitoring of a full-scale wind turbine blade using ultrasonic guided waves under varying temperature conditions,” *Structural control and health monitoring*, vol. 25, no. 4, p. e2138, 2018.
[9] A. Shah, O. Niksan, M. C. Jain, K. Colegrave, M. Wagih, and M. H. Zarifi, “Microwaves see thin ice: A review of ice and snow sensing using microwave techniques,” *IEEE Microwave Magazine*, vol. 24, no. 10, pp. 24–39, 2023.
[10] D. Kilani, F. Niknahad, A. Shah, S. Olsen, M. Meaker, and M. H. Zarifi, “Wireless microwave sensor network using split ring resonators for ice monitoring applications,” *IEEE Internet of Things Journal*, vol. 11, no. 14, pp. 25 316–25 325, 2024.
[11] A. Yousuf, H. Khawaja, and M. S. Virk, “A review of infrared thermography applications for ice detection and mitigation,” *Cold Regions Science and Technology*, vol. 218, p. 104058, 2024.
[12] L. M. Weinstein, “Ice detector,” Tech. Rep., 1988.
[13] M. C. Homola, P. J. Nicklasson, and P. A. Sundsbø, “Ice sensors for wind turbines,” *Cold regions science and technology*, vol. 46, no. 2, pp. 125–131, 2006.
[14] S. Evans, “Dielectric properties of ice and snow–a review,” *Journal of Glaciology*, vol. 5, no. 42, pp. 773–792, 1965.
[15] T. Yue, X. Wang, B. Wang, S. Tai, H. Liu, L. Wang, and F. Jiang, “Design of ice tolerance flight envelope protection control system for uav based on lstm neural network for detecting icing severity,” *Drones*, vol. 9, no. 1, p. 63, 2025.

[16] A. A. Jiménez, F. P. G. Márquez, V. B. Moraleda, and C. Q. G. Muñoz, "Linear and nonlinear features and machine learning for wind turbine blade ice detection and diagnosis," *Renewable energy*, vol. 132, pp. 1034–1048, 2019.
[17] M. Ayyad, M. Temimi, M. Abdelkader, M. M. Henein, F. L. Engel, R. R. Lotspeich, and J. R. Eggleston, "Rice-net: Integrating ground-based cameras and machine learning for automated river ice detection," *Environmental Modelling & Software*, vol. 190, p. 106454, 2025.
[18] K. L. Sørensen, A. S. Helland, and T. A. Johansen, "Carbon nanomaterial-based wing temperature control system for in-flight anti-icing and de-icing of unmanned aerial vehicles," in *2015 IEEE aerospace conference*. IEEE, 2015, pp. 1–6.
[19] D. Farina, H. Machrafi, P. Queeckers, P. D. Dongo, and C. S. Iorio, "Innovative ai-enhanced ice detection system using graphene-based sensors for enhanced aviation safety and efficiency," *Nanomaterials*, vol. 14, no. 13, p. 1135, 2024.
[20] A. Kovtun, E. Treossi, N. Mirotta, A. Scidà, A. Liscio, M. Christian, F. Valorosi, A. Boschi, R. J. Young, C. Galiotis *et al.*, "Benchmarking of graphene-based materials: real commercial products versus ideal graphene," *2D Materials*, vol. 6, no. 2, p. 025006, 2019.
[21] K. Lahbacha, S. Sibilia, G. Trezza, G. Giovinco, F. Bertocchi, S. Chiodini, F. Cristiano, and A. Maffucci, "Electro-thermal parameters of graphene nano-platelets films for de-icing applications," *Aerospace*, vol. 9, no. 2, p. 107, 2022.
[22] F. Siconolfi, G. Cavaliere, S. Sibilia, F. Cristiano, G. Giovinco, and A. Maffucci, "Industrial-grade graphene films as distributed temperature sensors," *Sensors*, vol. 25, no. 10, p. 3227, 2025.
[23] NANESA Srl, "Semilavorati e additivi," https://www.nanesa.it/semilavorati-e-additivi/#gpaper, 2025, accessed: 2025-09-15.
[24] G. Cavaliere, L. Tari, A. Maffucci, and L. Ferrigno, "High-performance nanocomposites for de-icing and de-snowing in photovoltaic applications," in *2025 IEEE International Conference on Environment and Electrical Engineering and 2025 IEEE Industrial and Commercial Power Systems Europe (EEEIC/I&CPS Europe)*. IEEE, 2025, pp. 1–6.
[25] S. Sibilia, F. Bertocchi, S. Chiodini, F. Cristiano, L. Ferrigno, G. Giovinco, and A. Maffucci, "Temperature-dependent electrical resistivity of macroscopic graphene nanoplatelet strips," *Nanotechnology*, vol. 32, no. 27, p. 275701, 2021.
[26] D. J. Adams, "Theory of the dielectric constant of ice," *Nature*, vol. 293, no. 5832, pp. 447–449, 1981.
[27] P. W. Rosenkranz, "A model for the complex dielectric constant of supercooled liquid water at microwave frequencies," *IEEE Transactions on Geoscience and Remote Sensing*, vol. 53, no. 3, pp. 1387–1393, 2014.
[28] M. Hallikainen, F. Ulaby, and M. Abdelrazik, "Dielectric properties of snow in the 3 to 37 ghz range," *IEEE transactions on Antennas and Propagation*, vol. 34, no. 11, pp. 1329–1340, 1986.
[29] B. Chen, D. Gao, J. Yang, and Z. Li, "Design of an active detection system for ice and snow pollutants and freezing temperature on runway," *Measurement Science and Technology*, vol. 34, no. 10, p. 105102, 2023.
[30] S. Sibilia, L. Tari, F. Bertocchi, S. Chiodini, and A. Maffucci, "A capacitive ice-sensor based on graphene nano-platelets strips," *Sensors*, vol. 23, no. 24, p. 9877, 2023.
[31] G. Sloggett, N. Barton, and S. Spencer, "Fringing fields in disc capacitors," *Journal of Physics A: Mathematical and General*, vol. 19, no. 14, p. 2725, 1986.
[32] M. Hosseini, G. Zhu, and Y.-A. Peter, "A new model of fringing capacitance and its application to the control of parallel-plate electrostatic micro actuators," *arXiv preprint arXiv:0711.3335*, 2007.
[33] H. B. Palmer, "The capacitance of a parallel-plate capacitor by the schwartz-christoffel transformation," *Electrical Engineering*, vol. 56, no. 3, pp. 363–368, 1937.
[34] S. Evans, "Dielectric properties of ice and snow–a review," *Journal of Glaciology*, vol. 5, no. 42, pp. 773–792, 1965.
[35] J. Xie, Z. Li, B. Lu, and W. Yuan, "A flexible csrr-based array icing sensor with defective microstrip structure," *IEEE Sensors Journal*, vol. 24, no. 12, pp. 19 934–19 943, 2024.
[36] L. Dong, Z. Zhang, H. Zheng, G. Yang, J. Hu, L. Shu, and X. Jiang, "Ice thickness/density measurement method based on its capacitance effect," *High Voltage*, vol. 10, no. 2, pp. 400–410, 2025.
[37] J. Xie, Z. Li, B. Lu, and W. Yuan, "A flexible csrr-based array icing sensor with defective microstrip structure," *IEEE Sensors Journal*, vol. 24, no. 12, pp. 19 934–19 943, 2024.
[38] D. Capriglione, C. Carissimo, F. Milano, A. Sardellitti, and L. Tari, "Measurement and applications: Artificial intelligence in the field of measurement applications," *IEEE Instrumentation Measurement Magazine*, vol. 27, no. 4, pp. 29–36, 2024.
[39] R. Andrian, M. Naufal, B. Hermanto, A. Junaidi, and F. R. Lumbanraja, "K-nearest neighbor (k-nn) classification for recognition of the batik lampung motifs," in *Journal of Physics: Conference Series*, vol. 1338, no. 1. IOP Publishing, 2019, p. 012061.
[40] L. Tari, C. Bourelly, M. Vitelli, F. Milano, M. Molinara, and L. Ferrigno, "A statistical approach for electrochemical impedance spectroscopy analysis on lfp batteries' state of charge," in *2023 IEEE International Workshop on Metrology for Industry 4.0 IoT (MetroInd4.0IoT)*, 2023, pp. 421–426.
[41] L. Tari, F. Milano, L. Ferrigno, A. Cesarano, D. Lanni, G. Erme, G. Ficco, G. Vuotto, and R. Ciampa, "A non-invasive measurement system for pollutant detection in oil: a preliminary analysis," in *2024 IEEE International Workshop on Metrology for Industry 4.0 IoT (MetroInd4.0 IoT)*, 2024, pp. 355–360.

Luca Tari (Member, IEEE) (luca.tari@unicas.it) was born in Cassino, Italy, in 1997. He is a research fellow at the Department of Electrical and Information Engineering, University of Cassino and Southern Lazio. He obtained his PhD in Methods, Models and Technologies for Engineering in December 2024, specializing in the field of electrical and electronic measurements with a focus on smart energy. He received his MSc (*cum laude*) in Electrical Engineering in October 2021 and his BSc (*cum laude*) in Industrial Engineering in July 2019 - both from the University of Cassino and Southern Lazio, Italy. His current research interests concern electrical and electronic measurements in the field of smart energy and energy digitization. In particular, the design and development of new methods and tools for smart monitoring, predictive diagnostics and cyber security. In addition, his research activities include the analysis of new distributed measurement systems and nanotechnology-based smart sensors for pollutant monitoring and ice detection in the aerospace and PV sectors.

Gabriele Cavaliere (Student Member, IEEE) (gcavaliere@unisa.it;gabriele.cavaliere@unicas.it), born in Cassino, Italy, in 1999, is a Ph.D. student at the University of Salerno for the National Ph.D. programme "Photovoltaics" since November 2023. In the same year, he obtained his master's degree (cum laude) in Electrical Engineering from the University of Cassino and Southern Lazio. His current research focuses on studying and implementing smart nanosensors within sensor networks to enable real-time monitoring of critical aspects of photovoltaic (PV) modules. Key areas of interest include fault detection and predictive diagnostics under specific environmental conditions in order to preserve the PV modules useful life. Additionally, his research extends to smart energy algorithms in PV systems.

Sarah Sibilia (Student Member, IEEE) (sarah.sibilia.unicas.it) was born in Benevento, Italy, in 1991. She received the B.Sc. and M.Sc. degrees in Electrical Engineering from the University of Cassino and Southern Lazio, Italy, in 2016 and 2019, respectively. From 2019 to 2022, she was a Research Fellow at the Department of Electrical and Information Engineering, University of Cassino and Southern Lazio; she is currently pursuing her Ph.D. at the same department, and she is working as electrical engineer at E-lectra srl, Cassino, Italy. Her main research interests concern multiphysics modeling and experimental characterization of nanomaterials and advanced electrical applications.

Antonio Maffucci (Senior Member, IEEE) (maffucci@unicas.it) (S'98-M'02-SM'11) received the Laurea Degree in Electronic Engineering summa cum laude in 1996 and the Ph.D. degree in Electrical Engineering in 2000, from the University of Naples Federico II, Italy. He is currently Full Professor of Electrotechnics with the Dept. of Electrical and Information Engineering at the University of Cassino and Southern Lazio, Cassino, Italy, and Research Associate at the National Institute of Nuclear Physics, INFN-LNF, Frascati, Italy. In 1997, he was with the nuclear fusion laboratory JET (Culham, U.K.). From 1998 to 2002, he was with the Dept. of Electrical Engineering, University of Naples Federico II. His research areas include computational electromagnetics, electromagnetic compatibility, distributed circuit and systems, nanoelectronics, and quantum circuits. He is author of about 200 technical papers on international journals, conference proceedings, books and essays on books. Prof. A. Maffucci is an Associate Editor of the IEEE Trans. on Components, Packaging, and Manufacturing Technology, a vice-chair of the IEEE EPS TC on Electrical Design, Modeling and Simulation, and a member of the IEEE Nanopackaging Council. He is also in the editorial boards of Applied Sciences and of Journal of Nanoscience and Nanotechnology Applications. He was the General Chairman of the conferences IEEE SPI 2011, 2012, and 2025, FANEM 2015 and 2018, and Terametanano 2024. He is the Coordinator of the EU-H2020 project "TERASSE".

Luigi Ferrigno (Senior Member, IEEE) (ferrigno@unicas.it) has been a Full Professor of electric and electronic measurement and the Scientific Manager of the Industrial Measurements Laboratory, University of Cassino, Cassino, Italy, since 2004. In 2008, he was a Founding Member of the university spin-off, Spring Off (University of Salerno), Fisciano, Italy. He is an NDE4.0 Ambassador for the Italian Association of Non-Destructive Evaluation and Test (AiPnD) in the EFNDT WG10. He coordinated and participated in several national and international research projects. His current research interests include the NDT4.0, novel learning sensors and measurement systems for smart city, the Internet of Things (IoT), automotive, smart energy, and environment.